$TlYbSe_2$ as a member of the $J=\frac{1}{2}$ triangular-lattice Yb delafossite family: From spin liquid to field-induced magnetic order

T. Fujii,[1] M. Pillaca,[2] F. Bärtl,[3,4] J. Sichelschmidt,[1] S. Luther,[3] H. Rosner,[1] A. M. Strydom,[5] J. Wosnitza,[3,4] H. Kühne,[3] Th. Doert,[2] and M. Baenitz[1,*]

[1]*Max Planck Institute for Chemical Physics of Solids, 01187 Dresden, Germany*

[2]*Faculty of Chemistry and Food Chemistry, TU Dresden, 01062 Dresden, Germany*

[3]*Dresden High Magnetic Field Laboratory (HLD-EMFL) and Würzburg-Dresden Cluster of Excellence ct.qmat, Helmholtz-Zentrum Dresden-Rossendorf, 01328 Dresden, Germany*

[4]*Institut für Festkörper- und Materialphysik, TU Dresden, 01062 Dresden Germany*

[5]*Highly Correlated Matter Research Group, Department of Physics, University of Johannesburg, P.O. Box 524, Auckland Park 2006, South Africa*

(Received 13 May 2025; accepted 8 July 2025; published 18 July 2025)

$TlYbSe_2$ is a new member of the Yb delafossite family, which differs strongly from the previously investigated alkali-metal Yb delafossites. It is characterized by a much larger saturation field (about 20 T) and a higher transition temperature (about 1.8 K) to the field-induced ordered state. As for the other Yb delafossites, long-range magnetic order is absent down to low temperatures at zero field. We report detailed macroscopic and microscopic measurements as a function of magnetic field and temperature to explore the $H-T$ phase diagram of polycrystalline $TlYbSe_2$. Besides bulk methods, such as magnetization and specific heat, spectroscopic methods, such as electron spin resonance (ESR) and nuclear magnetic resonance (NMR), are applied. The magnetic anisotropy can be determined by means of these microscopic probes; in particular, Yb-ESR and Se-NMR are powerful tools here. The magnetization, ESR, and NMR data evidence a large anisotropy factor of about 10 for the ratio of the magnetic moment in the Yb-Se triangular-lattice plane and perpendicular to it. Such a strong spin anisotropy was only found in $CsYbSe_2$, which identifies both systems as prototype two-dimensional triangular-lattice spin liquids. Even though $CsYbSe_2$ shares the same spin anisotropy, it has a much smaller magnetic exchange coupling between the Yb moments than $TlYbSe_2$, which leads to a field-induced ordering at much lower temperatures (1 K) and a smaller saturation field of only 10 T. We speculate that this originates from the use of thallium as a monovalent cation (Tl^{+1} with $[Xe]4f^{14}5d^{10}6s^2$) instead of the intensively studied alkali metals (Na^{+1}, K^{+1}, Rb^{+1}, Cs^{+1}) with completely filled (Ne, Ar, Kr, Xe) shells. In particular, the emergence of a Tl^{+1}-based lone-pair $6s^2$-Se-$4p$ polarization might have a strong impact on the strength and anisotropy of the magnetic exchange among the Yb ions in the $TlYbSe_2$ lattice. In contrast to that, the spin anisotropy of the pseudo-spin-1/2 Yb ions remains unaltered by the presence of Tl $6s^2$ lone pairs.

DOI: 10.1103/lkqb-3fc7

I. INTRODUCTION

The delafossite structure with its ideal planar arrangement of trivalent ions represents a perfect realization of the triangular lattice [1,2]. Unlike other systems, there is no inherent disorder. While magnetic $3d$ delafossites with Cr or Fe have been extensively studied [3,4], there is an increasing interest in compounds with trivalent $4f$ ions. In particular, the Kramers ion Yb is of special interest and Yb delafossites are now established as an intriguing class of triangular-lattice spin-liquid systems [5–10]. Due to the complex ground state of the Yb ion and the resulting bond-dependent superexchange via p states of the chalcogens, strong frustration occurs, which completely suppresses ordering [9]. With the application of a magnetic field, the frustration is released and magnetic order is induced. In a magnetic field, magnetic textures are found, which are also known from other more classical spin-1/2 triangular lattices with d ions [11].

It is striking that alkali-metal Yb delafossites (such as $NaYbCh_2$, with $Ch = O, S, Se$) all show a similar phase diagram. Important characteristics here are the maximum ordering temperature of about 1 K and the saturation field into the polarized state of about 15 T. This suggests that the frustration is similar in all these systems [9]. Furthermore, in principle, it should be possible to drive the systems into a magnetically ordered state by chemical doping or applying pressure, but this has not been achieved so far.

We have now succeeded in finding a Yb delafossite, which is also a spin liquid with field-induced order, but which is

*Contact author: michael.baenitz@cpfs.mpg.de

Published by the American Physical Society under the terms of the Creative Commons Attribution 4.0 International license. Further distribution of this work must maintain attribution to the author(s) and the published article's title, journal citation, and DOI. Open access publication funded by Max Planck Society.

clearly different from the alkali-metal Yb-based spin liquids. Besides the alkali metals, there are a few other monovalent ions in the periodic system (for instance, Ag and Tl). Compared to simple alkali metals such as Li, Na, and K, Tl has a larger ionic radius, which means that the c axis in $TlYbSe_2$ is larger than in $NaYbSe_2$. This means that the triangular planes in $TlYbSe_2$ are also significantly further apart, which pushes the system more in the direction of a two-dimensional (2D) quantum magnet. The ionic radius of Tl, on the other hand, is comparable to that of Rb or Cs. For $CsYbSe_2$, the largest magnetic anisotropy in the Yb-delafossite family appears in the electron spin resonance (ESR) g factor, which clearly indicates a 2D behavior [12,13].

Furthermore, the electronic configuration of Tl^{+1} provides $6s^2$ lone pairs. Similar to Yb^{+3}, Tl^{+1} has an octahedral coordination in the $TlSe_6$ unit and a lone-pair $6s^2$-Se-$4p$ polarization might occur. This seems to tune the magnetic exchange and strengthen the antiferromagnetic correlations. Tl-based $6s^2$ lone pairs polarize the spatially extended Se-based $4p$ states, which might have an impact on the coupling between the Yb-Se-Yb triangular layers. We propose that the coupling between the layers is enhanced due to a hybridization of Tl-based $6s^2$ orbitals with Se-based $4p$ orbitals, which finally reduces the overall exchange anisotropy in the $TlYbSe_2$ system. Thus, the exchange interaction is more likely to have a three-dimensional character, whereas the spin anisotropy remains two dimensional. Interestingly, the strong frustration and the spin-liquid ground state are preserved.

$TlYbCh_2$ (Ch denotes a chalcogen) systems have rarely been studied in detail. There is only one study on the magnetization of $TlYbS_2$ single crystals [14]. In contrast to $TlYbSe_2$ with an $R\bar{3}m$ space group, this system belongs to the $P6_3$ space group. Interestingly, there are no signs of magnetic order above 0.4 K and in fields up to 7 T from magnetization measurements [14].

Here we present detailed investigations of polycrystalline $TlYbSe_2$ with $R\bar{3}m$ symmetry. We will show that the spin anisotropy is comparable to that of $CsYbSe_2$ and $NaYbSe_2$, but the antiferromagnetic coupling between the Yb moments is significantly stronger, resulting in a much more robust field-induced magnetic state, an increased transition temperature, and a larger saturation field. At the same time, the frustration is preserved, so that at low temperatures, we find a spin-liquid state without magnetic order. Due to the stronger antiferromagnetic coupling, we conclude that the frustration is significantly larger compared to $CsYbSe_2$ [12,13] or $NaYbSe_2$ [7]. This makes Tl-based Yb-Ch_2 systems a different subgroup of triangular-lattice quantum spin liquids (QSLs).

II. EXPERIMENT

A. Methods

The magnetization measurements in static fields were performed using a superconducting quantum interference device (SQUID) vibrating sample magnetometer from Quantum Design. The magnetization measurements in pulsed magnetic fields up to 60 T were performed at the Dresden High Magnetic Field Laboratory (HLD), using a compensated pickup-coil magnetometer in a ^{4}He cryostat and a pulsed magnet with an inner bore of 20 mm, powered by a 1.44 MJ capacitor bank [15]. The specific-heat measurements were conducted using a physical property measurement system from Quantum Design.

We investigated the electron spin resonance (ESR) of single-crystalline as well as polycrystalline $TlYbSe_2$. The ESR of a paramagnetic sample in a magnetic field H is probed by detecting the power absorbed by a transversal applied magnetic microwave field h_{mw} due to resonance with the Zeeman-split spin levels. For improved signal-to-noise ratio, the first field derivative of absorbed microwave power, dP/dH, is recorded. We used a continuous-wave ESR spectrometer at X-band (9.4 GHz) microwave frequency. For sample cooling, a ^{4}He-flow cryostat was employed to reach temperatures down to 2.5 K. The measured resonance spectra were described with a Lorentzian shape, yielding the parameters' linewidth ΔH, resonance field H_{res}, and amplitude. These parameters allow one to calculate the static spin-probe magnetic susceptibility χ_{ESR} along the microwave magnetic field [16].

Field-sweep nuclear magnetic resonance (NMR) measurements were carried out using the conventional pulsed NMR technique on the ^{77}Se and ^{203,205}Tl nuclear isotopes (all with nuclear spin $I = 1/2$) at temperatures between 2 and 295 K and at various magnetic fields. The powder was mixed with paraffin in a small quartz tube, subsequently heated, shaken, and then cured to randomize the grain orientations. The field-sweep spectra are obtained by integration over the spin echo in the time domain at a given field. The powder spectra are analyzed using an anisotropic shift tensor. The NMR shift components in the a-b plane and the c direction perpendicular to the plane are determined from the fits to the spectra. AC-susceptibility measurements were done using the magnetic measurement option in a dilution refrigerator insert on a Dynacool cryogenic station from Quantum Design. In the format of a compressed pellet, the sample was secured using GE varnish onto a quartz pedestal attached to the mixing chamber stand-off. The sample was located inside an AC-drive coil which was charged to an alternating field of amplitude 0.3 mT and frequency 10 kHz. While cooling the sample, the temperature was stabilized at each individual data point before collecting data of the induced magnetic moment.

B. Synthesis of polycrystalline material

High-purity elements of thallium (Alfa Aesar, 99.9%, rod), ytterbium (Mateck, 99.99%, rod), and selenium (Chempur, 99.999%, chunks) were used as starting materials. Selenium was reduced in a hydrogen flow at 400 °C. Due to the air sensitivity of the starting materials, the handling of these materials and products was carried out in a glove box with O_2 and H_2O levels below 0.1 ppm. Polycrystalline $TlYbSe_2$ samples were obtained in a two-stage reaction, adapting synthetic approaches reported earlier [17,18]. Tl_2Se as a precursor was prepared from a stoichiometric mixture of thallium and selenium in an evacuated glass ampule (1×10^{-3} mbar) at 500 °C for 24 hours. In a second step, $TlYbSe_2$ was synthesized from a mixture of Tl_2Se:Yb:Se in a molar ratio of 1:2:3, respectively. These three components were mixed in an agate mortar and filled in a glassy carbon crucible inside a quartz ampoule

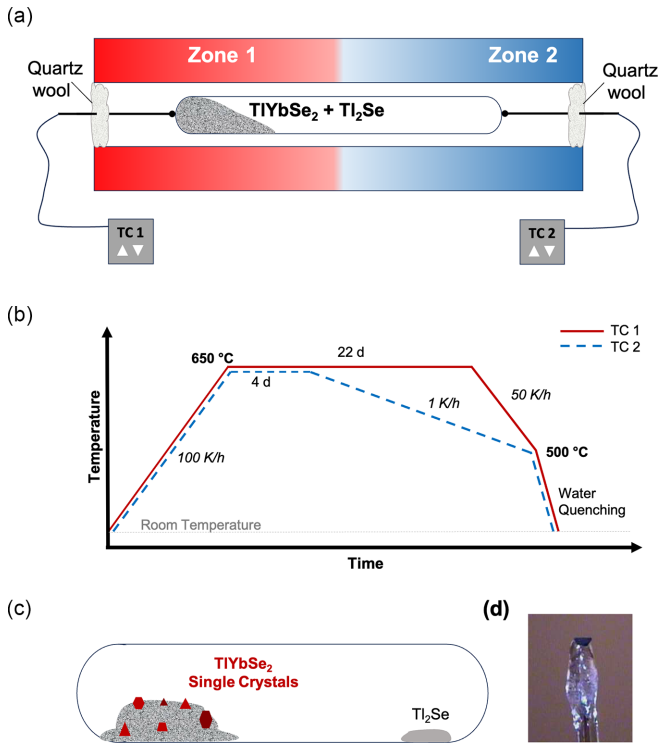


FIG. 1. (a) Sketch of the experimental setup to grow single crystals of TlYbSe$_2$. (b) Temperature program used during the sample growth and (c) schematic illustration of the ampoule after growth. (d) Close-up of a TlYbSe$_2$ single crystal mounted for a x-ray diffraction measurement.

of 16 mm outer diameter. After flame sealing under vacuum, the ampoule was placed in a furnace and heated to 500–540 °C with a rate of 100 K/h for 24 hours.

C. Single-crystal growth

Single crystals of TlYbSe$_2$ were grown by a modified version of the self-selecting vapor growth (SSVG) procedure of bulk crystals [19,20]. The single crystals were grown in a horizontal two-zone furnace by using an excess of Tl$_2$Se. Polycrystalline TlYbSe$_2$ and Tl$_2$Se in a mass ratio of 1:3.5, respectively, were introduced in a quartz ampule of 1.6 cm diameter and 13 cm length. After evacuating, the ampule was sealed and placed in the center of a two-zone furnace, as shown in Fig. 1(a). Two external thermocouples were placed at the ends of the ampule to monitor the temperatures. The detailed temperature program used in this work is shown in Fig. 1(b). After approximately three weeks, small red, platelet-shaped TlYbSe$_2$ crystals were observed on top of the powder, as is shown in the schematic illustration in Fig. 1(c). At the other end of the ampule, some of the excess of Tl$_2$Se condensed. The resulting single crystals varied in appearance and size, with the typical size, however, being about $0.5 \times 0.4 \times 0.1$ mm^3. The dark-red single crystals were found to consist of several platelets growing on top of each other. An image of a single crystal of TlYbSe$_2$ with a trapezoidal shape, mounted for a diffraction experiment, is shown in Fig. 1(d).

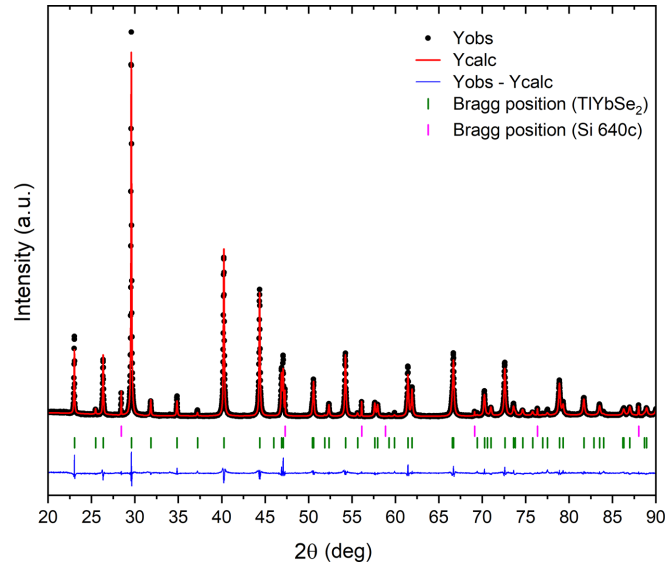


FIG. 2. PXRD pattern with Rietveld refinement for a polycrystalline TlYbSe$_2$ sample. Solid black circles and red lines indicate the observed and calculated intensities, respectively. Short vertical lines indicate the position of Bragg reflections for TlYbSe$_2$ and the internal Si standard. The blue lines show the difference between the observed and calculated intensities.

D. X-ray diffraction measurement

The powder x-ray diffraction (PXRD) pattern of the polycrystalline sample was collected at room temperature on a PANalytical Empyrean diffractometer with Cu-Kα_1 radiation ($\lambda = 1.5406$ Å), equipped with a Ge(111) monochromator. For the accurate lattice-parameter determination, the sample was mixed with a small amount of Si powder (NIST SRM 640c) as an internal standard. The Rietveld refinement analysis of the PXRD pattern was done with the fundamental parameter approach using the TOPAS Academic software package [21,22]. The isotropic temperature factors B_{eq} were kept fixed at 1.0 Å^2 and the site occupancies were also fixed to 1.0. The single-crystal x-ray diffraction (SCXRD) data collection on suitable single crystals was performed using Mo-K$_{\alpha 1}$ radiation ($\lambda = 0.71073$ Å) on a Bruker Apex-II diffractometer, equipped with a CCD detector utilizing a graphite (002) monochromator. The Bruker APEX3 software suite was used for the measurement, evaluation, data reduction, and absorption correction [23]. The structure solution and refinement were carried out using the SHELX software package [24,25]. Energy-dispersive x-ray spectroscopy (EDX) on single crystals and chemical analysis by inductively coupled plasma optical emission spectroscopy (ICP-OES), measured on several batches of the TlYbSe$_2$ polycrystalline samples, confirm the stoichiometric composition of the delafossite compound.

III. RESULTS AND DISCUSSION

A. Crystal structure

The PXRD pattern of the polycrystalline TlYbSe$_2$ sample and the result of the Rietveld fit are shown in Fig. 2. All diffraction peaks can be assigned to the trigonal crystal structure and space group $R\bar{3}m$ (No. 166). The obtained lattice

TABLE I. Structure-refinement results for a red-platelet single crystal of $TlYbSe_2$. The data were collected on a Bruker Apex-II CCD diffractometer with Mo-K_α radiation of $\lambda = 0.71073$ Å.

Empirical formula	$TlYbSe_2$
Formula weight (g/mol)	535.33
Temperature (K)	298.06
Crystal system	Trigonal
Space group	$R\bar{3}m$ (No. 166)
Z	3
a (Å)	4.0788(3)
c (Å)	23.1260(16)
V (Å^3)	333.19(5)
Atomic position z (Se^{2-})	0.2658(3)
Density calculated (g/cm^3)	8.004
Absorption coefficient (mm^{-1})	73.31
$F(000)$	657.0
θ range (°)	2.64–38.41
Data/parameters/restraints	280/9/0
Index ranges	$-7 \leqslant h \leqslant 6$ $-7 \leqslant h \leqslant 7$ $-39 \leqslant h \leqslant 39$
Reflections collected	3145
Independent reflections	271
Goodness of fit on F^2	1.198
Final R indexes [$I > 2\sigma(I)$]	$R_1 = 0.0219$, $wR_2 = 0.0520$
Final R indexes (all data)	$R_1 = 0.0223$, $wR_2 = 0.0520$
Largest diff. peak/hole (e^-/Å^3)	2.53/−3.14
Completeness (%)	100.0

parameters $a = 4.07895(3)$ Å, $c = 23.1421(2)$ Å, and $V = 333.451(6)$ Å^3 are in good agreement with the literature data [18]. SCXRD data collection and structure-refinement details for $TlYbSe_2$ are summarized in Tables I and II. These results also confirm the Rietveld results and the literature data [18]; see Table III.

B. DFT band structure calculations

Figure 3 (top) shows a comparison of the total electronic density of states (DOS) of $AYbSe_2$ for the formally monovalent cations A = Na, K, Rb, and Tl. Whereas, for the alkaline ions, the DOS's are very similar, as expected due to the similar crystal structures and formal charges, the Tl compound shows a much larger valance bandwidth and a significantly narrower band gap. Although the c axis of the alkaline compounds is significantly different within the series, the bandwidth is almost the same. The underlying reason is that the coupling between the $YbSe_2$ layers is small, leading to a small band dispersion along c and thus only to minor differences in the overall band dispersion among these systems. In contrast, the valence bandwidth of the Tl system is almost twice as large as that of the K compound, which has the most similar lattice parameters compared to $TlYbSe_2$.

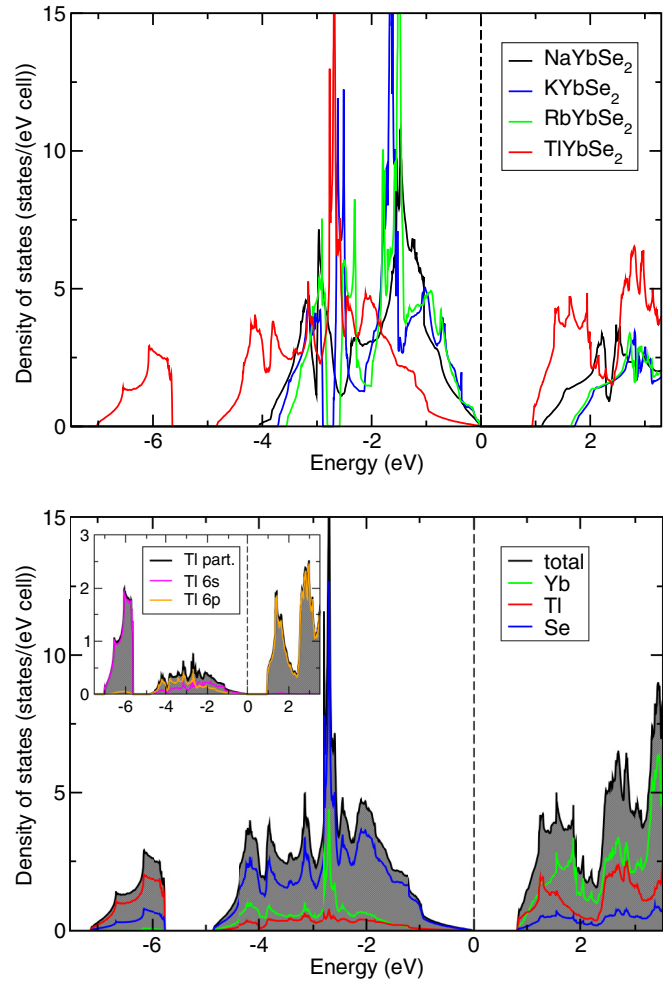


FIG. 3. Total and partial electronic density of states (DOS) of $TlYbSe_2$ (bottom). The Fermi level at zero energy is given by a dashed line. Inset: The dominating orbital contributions of the partial Tl DOS. The top panel shows a comparison of the $TlYbSe_2$ total DOS with that of the isostructural compounds, where the alkaline ions Na, K, and Rb replace Tl.

To analyze the origin in more detail, in Fig. 3 (bottom), the partial DOS of $TlYbSe_2$ is plotted. We can separate two features that show the main differences: (i) the Tl "lone-pair" related states between about −5.5 and −7 eV binding energy

TABLE II. Anisotropic (U_{ij}) and isotropic (U_{eq}) displacement parameters (in 10^3 Å^2) for $TlYbSe_2$, determined from the refinement of the SCXRD data. The anisotropic-displacement factor takes the form $-2\pi^2(U_{11}h^2a^{*2} + U_{22}k^2b^{*2} + U_{33}l^2c^{*2} + 2\,U_{12}hka^*b^* + 2\,U_{13}hla^*c^* + 2U_{23}klb^*c^*)$.

Atom	U_{11}	U_{22}	U_{33}	U_{23}	U_{13}	U_{12}
Yb	7.89(14)	7.89(14)	9.59(18)	0	0	3.94(7)
Tl	21.89(16)	21.89(16)	21.1(2)	0	0	10.95(8)
Se	9.31(18)	9.31(18)	8.7(3)	0	0	4.65(9)

TABLE III. Atomic coordinates and equivalent isotropic displacement parameters B_{eq} for TlYbSe$_2$.

Atom	Wyckoff position	PXRD data refinement					SCXRD data refinement				
		x	y	z	Occ.	B_{eq}(Å^2)	x	y	z	Occ.	B_{eq}(Å^2)[a]
Yb	3*a*	0	0	0	1.0	1.0	0	0	0	1.0	0.667(10)
Tl	3*b*	0	0	1/2	1.0	1.0	0	0	1/2	1.0	1.706(11)
Se	6*c*	0	0	0.2656(5)	1.0	1.0	0	0	0.2658(3)	1.0	0.719(13)

[a]B_{eq} is calculated as $B_{eq} = 8\pi^2 U_{eq}$, where U_{eq} is defined as 1/3 of the trace of the orthogonalized U_{ij} tensor (see corresponding values in Table II).

and (ii) the pronounced "foot" between −1 eV and the Fermi level. Without these features, the TlYbSe$_2$ DOS would be rather similar to the alkaline family. The "lone-pair" states are rather broad due to a strong hybridization between Tl and Se, visible by the mixed character in the partial DOS. The inset shows that for Tl, essentially only the 6*s* states contribute as one would expect from a lone pair; for Se, the contribution is mainly due to its 4*p* states (not shown). The "foot" at the top of the valence band is a consequence of this hybridization as well. The respective antibonding Tl-6*s* Se-4*p* hybrid states are pushed up near the Fermi level. Closer inspection of the related bands (see the Appendix) shows a sizable dispersion perpendicular to the YbSe2 planes; in this way, mediating an increased interaction between them and consequently leading to larger magnetic couplings.

C. Susceptibility: Temperature and field dependence

Figure 4 shows the susceptibility of polycrystalline TlYbSe$_2$ as a function of temperature in a magnetic field of 0.1 T. Above approximately 80 K, the susceptibility $\chi(T)$ can be well described using a combination of a Curie-Weiss-type temperature-dependent contribution and a temperature-independent Van Vleck–like contribution:

$$\chi(T)|_{T\geqslant 80\,\mathrm{K}} = \chi_{VV} + \frac{N_A \mu_0}{3}\frac{\mu_{eff}^2}{T-\Theta}. \quad (1)$$

This yields a Curie-Weiss (CW) temperature of $\Theta = -73$ K and an effective moment of $\mu_{eff} = 4.5\mu_B$. The μ_{eff} value agrees with the theoretical prediction for trivalent Yb with $J = 7/2$ ($4.54\mu_B$).

The low-T susceptibility below about 50 K can be described similarly, which leads to $\Theta = -25$ K and $\mu_{eff} = 3\mu_B$. While for the high-temperature fit (CW1), the temperature-independent susceptibility contribution was a free fit parameter, for the low-temperature fit (CW2), we used the results of the high-field magnetization measurement up to 45 T at 2 K (see Fig. 5). Above 30 T, the Van Vleck susceptibility is determined from the linear $M(H)$ dependence. The single-crystal ESR study presented in Sec. III E yields a powder-averaged effective moment of $\mu_{ESR} \simeq g_{av}\sqrt{J(J+1)} \simeq 2.34\mu_B$, which is smaller than the value obtained from the low-temperature CW fit ($3\,\mu_B$) on the polycrystalline sample. This deviation can possibly be explained by partially aligned areas in the polycrystalline sample. Here the averaging over all directions in the powder for the determination of the Van Vleck contribution may not be the best correction. In contrast to

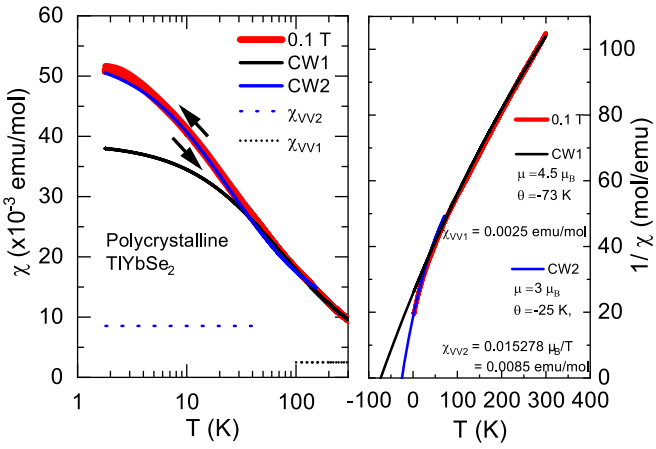


FIG. 4. Susceptibility (left) and inverse susceptibility (right) as a function of temperature, measured at a magnetic field of 0.1 T. The lines represent fits with a Curie-Weiss term and a constant Van Vleck susceptibility at different temperature regimes (CW1: above about 80 K; CW2: below about 50 K). The arrows indicate whether measurements were taken during warming up (zero-field cooling) or cooling down (field cooling).

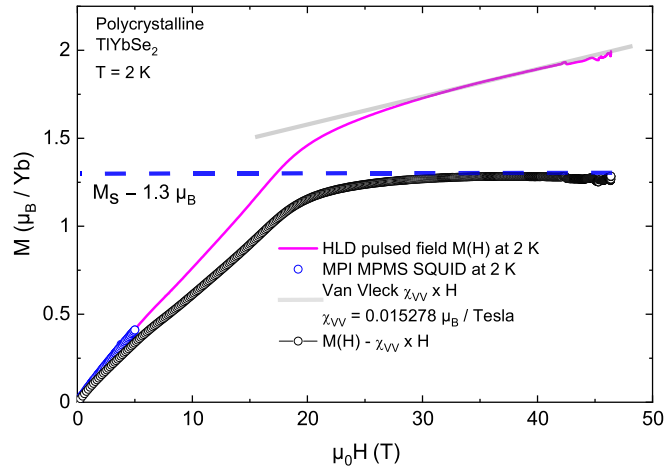


FIG. 5. Magnetization vs field at $T = 2$ K. The open symbols represent data from SQUID measurements, and the pink solid line represents high-field magnetization data recorded in pulsed fields. The solid gray line corresponds to the linear Van Vleck contribution ($M_{VV} = H\chi_{VV}$). The dashed horizontal line indicates the saturation magnetization, which is in good agreement with the value determined from the ESR g factors by $M_{sat} = g_{av}J_{eff}\mu_B$.

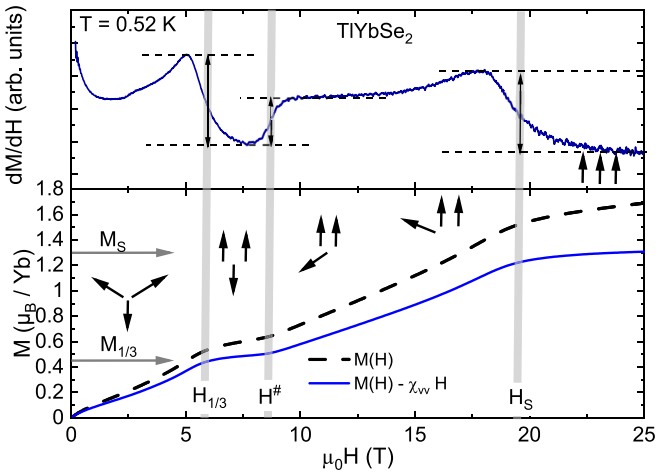


FIG. 6. Magnetization vs field at $T = 0.52$ K (bottom). The dashed line represents the uncorrected pulsed-field magnetization data, whereas the solid line correspond to the Van Vleck–corrected magnetization data [$M(H)$ - $H\chi_{VV}$]. The top panel shows the first derivative of the magnetization as a function of field. The inflection points (maximum in second derivative) indicate crossovers between the 120 degree magnetic order to the up-up-down (uud) order, canted uud variants, and, finally, the field-polarized phase.

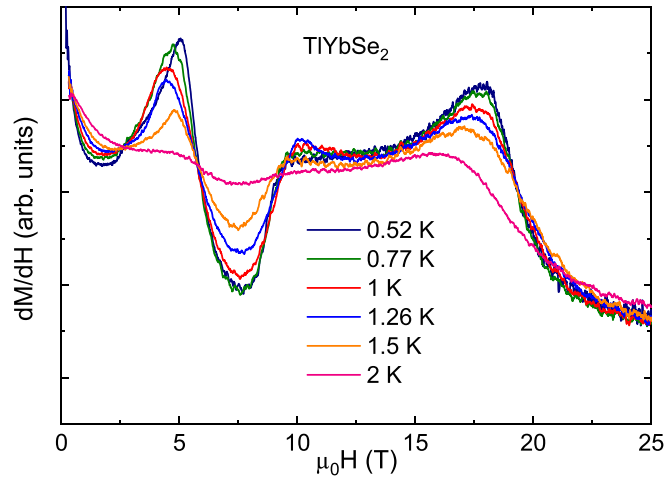


FIG. 7. Derivative of the magnetization vs field at various temperatures as indicated.

that, the Curie-Weiss temperature of $\Theta = -25$ K from our susceptibility fit (CW2) is in good agreement with the Curie-Weiss temperature determined from the ESR intensity ($\Theta = -22$ K) in the same temperature range (Fig. 8). A comparison with results on the single crystal of the related homologous compound $NaYbSe_2$ ($\Theta = -7$ K for in-plane field and $\Theta = -3.5$ K for field perpendicular to it [7]) shows that the Curie-Weiss temperature for $TlYbSe_2$ is significantly larger. This allows the general conclusion that there is a much stronger antiferromagnetic coupling among the Yb moments in the $TlYbSe_2$ triangular lattice.

D. High-field magnetization

Figure 5 shows the isothermal magnetization as a function of the magnetic field at 2 K. Here, the blue open circles represent data taken using a SQUID magnetometer up to 5 T, and the pink solid line represents data taken in a pulsed field up to 45 T. Above about 30 T, a linear magnetization is observed. The Van Vleck contribution to M can be determined from the linearity. After subtraction of the Van Vleck contribution, the saturation magnetization $M_{sat} = g_{av} J_{eff} \mu_B = 1.3\mu_B$ allows the determination of an averaged value of $g_{av} = 2.6$. ESR measurements on a single crystal result in a value of $g_{av} = \sqrt{(g_\parallel^2 + 2g_\perp^2)/3} \simeq 2.71$, which is in good agreement with the g factor obtained from the magnetization. At low temperatures, the $M(H)$ curves give strong evidence for field-induced effects. The isothermal magnetization (Fig. 6) measured at $T = 0.52$ K shows a clear plateau between 6 and 8 T at about one-third of the saturation magnetization, $M_{1/3} \simeq 0.43\mu_B$. The $M_s/3$ plateau is a strong indication for the emergence of an up-up-down (uud) bound-state spin arrangement, which is predicted by mean-field theory for the planar triangular lattice [11]. Upon further increasing the magnetic field, an up-up-canted-down and, finally, a fully polarized spin state (uuu) evolve. The crossover fields between the various spin orientations could be determined by a detailed analysis of the first derivative of the magnetization as a function of field (Figs. 6 and 7). We have already used this procedure to analyze the magnetization of the related homologous compound $NaYbSe_2$ [7]. We determined the crossover fields for the $H - T$ phase diagram as well using temperature- and field-dependent specific-heat and nuclear magnetic resonance studies.

E. Electron spin resonance

The electron spin resonance of Yb^{3+} spins on a triangular lattice has proven to provide local information on the g factor and on the spin dynamics of potential QSL systems [26–29]. It was shown that the anisotropic exchange interaction between the spins has a major impact on the ESR linewidth. At the lowest temperatures, critical spin dynamics, following a power law, determine the ESR linewidth. The local spin susceptibility could be determined from the ESR intensity, which confirms the results of the bulk-susceptibility measurements. Towards high temperatures, relaxation contributions from the first excited crystal-field level of Yb^{3+} dominate the linewidth. All these properties can as well be found for the ESR in $TlYbSe_2$.

We investigated the ESR of both single crystals and polycrystalline powder of $TlYbSe_2$ in order to check consistencies of the ESR parameters between both forms of material. Figure 8 shows the spectra at selected temperatures together with Lorentzian line fittings. The ESR g values, as determined via the resonance condition, are strongly anisotropic. The ratio of $g_\perp/g_\parallel \simeq 9.22$ is comparable to what is found for $CsYbSe_2$ ($g_\perp/g_\parallel \simeq 10.83$) [12] and evidences a strong spin anisotropy in both cases. Se-NMR results on $TlYbSe_2$ (see Sec. III F) provide an anisotropy ratio of $K_\perp/K_\parallel \simeq 11$ at 2 K, which is in reasonable agreement with the g-factor anisotropy from ESR, $g_\perp/g_\parallel \simeq 9.22$. It must also be mentioned that the ESR anisotropy factor is also significantly larger than in the well-studied $NaYbSe_2$ system, where $g_\perp/g_\parallel \simeq 3$ was found

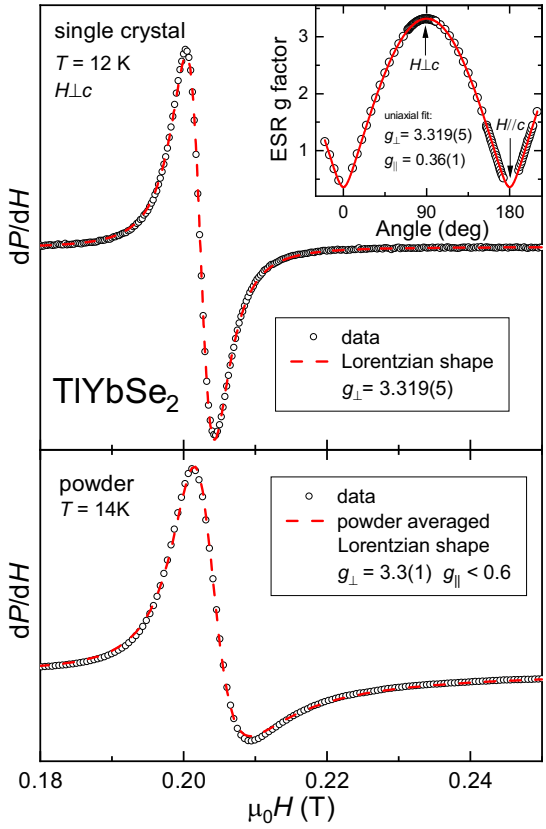


FIG. 8. Typical ESR spectra of $TlYbSe_2$. Dashed lines denote Lorentzian line shapes. Top panel: ESR spectrum of a single crystal for the external field H applied within the ab plane. For out-of-plane field orientations, the inset shows the anisotropy of the ESR g factor. The solid line indicates $g(\phi) = \sqrt{g_\parallel^2 \sin^2\phi + g_\perp^2 \cos^2\phi}$, with $g_\parallel = 0.36(1)$ and $g_\perp = 3.319(5)$. Lower panel: ESR spectrum of a powder sample with powder-averaged Lorentzian line fit, yielding anisotropic g values as indicated.

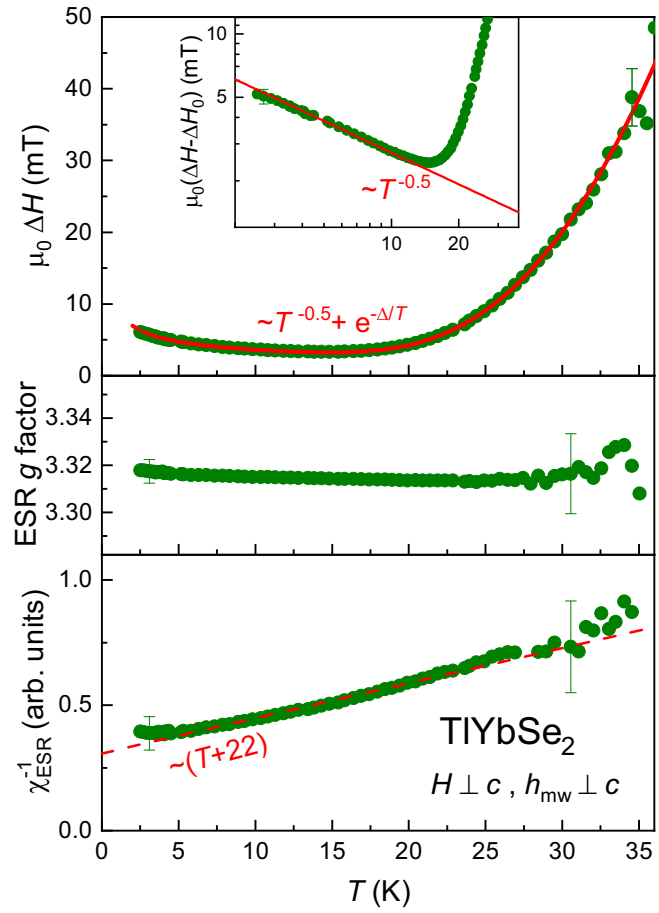


FIG. 9. Temperature dependences of the linewidth ΔH, ESR g factor, and the intensity $I_{\rm ESR} \equiv \chi_{\rm ESR}^{-1}$. Top panel: Towards low temperatures, $\Delta H(T) - \Delta H_0$ is consistent with a power law $\propto T^{-0.5}$ (see inset, constant offset $\Delta H_0 = 0.9$ mT), whereas at high temperatures, an exponential behavior reflects a relaxation via the first excited crystalline-electric-field level of Yb^{3+} at $\Delta = 150 \pm 15$ K. Middle panel: The ESR g factor is temperature independent within experimental error. Bottom panel: Reciprocal Yb^{3+} spin susceptibility $\chi_{\rm ESR}^{-1}$. The dashed line denotes a Curie-Weiss behavior with $\Theta = -22$ K.

[7] (and in the Se-NMR shift, a value of $K_\perp/K_\parallel \simeq 2$ [30]). The dependence of the ESR g factor on the orientation of the external field is uniaxial regarding an out-of-plane crystal rotation, as depicted in the inset of the top frame of Fig. 8. Such uniaxial symmetry of the ESR spectra leads, in the case of powder samples, to an averaged Lorentzian line shape, as indicated by the solid line in the bottom frame of Fig. 8, in good agreement with the experimental powder-sample ESR data. The larger linewidth compared to the single-crystal line can be understood due to additional relaxation channels, such as those due to grain boundaries.

Figure 9 shows the temperature dependencies of the ESR parameters for the in-plane orientation $H \perp c$ and $h_{\rm mw} \perp c$. For the orientation $H \| c$, the linewidth is unmeasurably broad. Towards low temperatures, the growing influence of spin correlations leads to an increase of the linewidth. In contrast to other Yb^{3+} triangular-lattice compounds, the power-law behavior $T^{-\alpha}$ of the linewidth is more in line with $\alpha = 0.5$ than $\alpha = 0.75$ [28]. Such a power-law increase of the linewidth is due to a suppression of exchange narrowing by classical critical fluctuations of a 3D order parameter [31,32]. Towards high temperatures, an Orbach process [33,34] dominates the broadening according to $1/[\exp(\Delta/T) - 1]$, with Δ denoting the first excited crystalline-electric-field level of Yb^{3+}. We obtained $\Delta = 150 \pm 15$ K (13 ± 1 meV), which is slightly smaller than what was found for $NaYbSe_2$ [28]. The temperature dependence of the g factor is very weak and can be considered constant within experimental error, as was similarly found in other Yb^{3+} triangular-lattice compounds [28]. The in-plane Yb^{3+}-spin susceptibility, as determined by the ESR intensity, $\chi_{\rm ESR}^{-1}$, shows a Curie-Weiss behavior with a Curie-Weiss temperature of $\Theta = -22$ K. For the related system $CsYbSe_2$, one finds $\Theta = -11.5$ K [12] and $\Theta = -14.3$ K for $NaYbSe_2$ [7]. The value $\Theta = -22$ K is in good agreement with the susceptibility data on polycrystalline $TlYbSe_2$ (see Sec. III B), which indicates the emergence of a much stronger antiferromagnetic coupling among the Yb moments in the new compound.

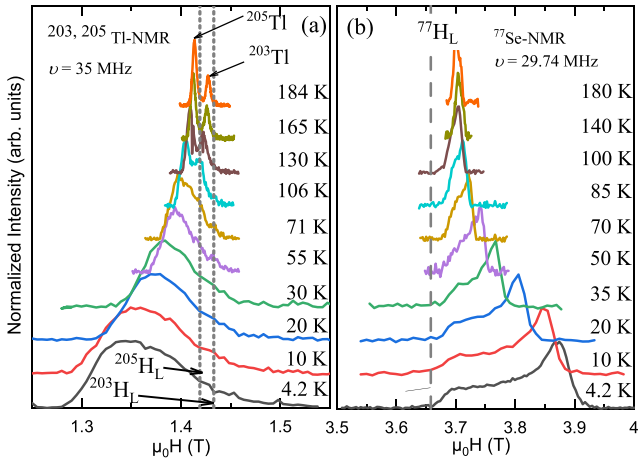


FIG. 10. (a) Tl- and (b) Se-NMR spectra of polycrystalline $TlYbSe_2$ at various temperatures. The spectra are normalized to the maximum value and shifted vertically with a constant offset at each temperature. Vertical dotted lines indicate the Larmor resonance fields H_L for ^{203}Tl, ^{205}Tl, and ^{77}Se.

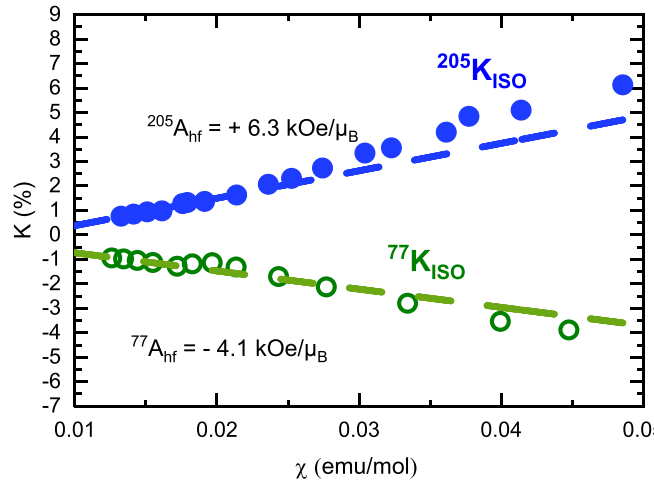


FIG. 11. $^{205}K_{\rm iso}$ (closed circles) and $^{77}K_{\rm iso}$ (open circles) vs powder susceptibility with temperature as the implicit parameter. The dotted lines are linear fits to the data above 100 K.

F. ^{77}Se and ^{203,205}Tl nuclear magnetic resonance

In order to obtain microscopic information on $TlYbSe_2$, ^{203}Tl, ^{205}Tl, and ^{77}Se are suitable nuclear isotopes to conduct the NMR measurements. These isotopes all have a nuclear spin $I = 1/2$; hence, no nuclear quadrupole interaction is present. The local fields at the Tl and Se sites originate from the Yb ($4f$ orbitals) - Se ($4p$ orbitals) transferred hyperfine interaction for the Se nuclei within the triangular plane, and from the Yb-Se-Tl-Se-Yb supertransferred hyperfine interaction for the Se and Tl nuclei. $TlYbSe_2$ belongs to the space group $R\bar{3}m$, in which the Tl and Se sites have trigonal symmetry and an uniaxial anisotropy of the hyperfine interaction is predicted for both sites. Therefore, the analysis of Tl- and Se-NMR spectra and nuclear magnetic relaxation data provide us with the local static and dynamic magnetic properties of the Yb moments.

The field-sweep Tl- and Se-NMR spectra at several temperatures are shown in Figs. 10(a) and 10(b), respectively. Those spectra were taken at frequencies of $\nu = 35.00$ MHz for Tl and 29.74 MHz for Se. Note that Tl has two isotopes with very similar nuclear gyromagnetic ratios γ. Hence, the NMR spectra split into two lines with intensities corresponding to the natural abundance (see Table IV). Both the Tl- and Se-NMR spectra show a powder pattern associated with the uniaxial distribution of the hyperfine fields because of the trigonal symmetry along the c axis. Accordingly, the hyperfine interaction produces an angular dependence of the resonance field according to $H_r(\theta) = \nu\gamma[1 + K_{\rm iso} + K_{\rm ax}(3\cos^2\theta - 1)]$,

TABLE IV. NMR-related parameters of ^{203,205}Tl and ^{77}Se.

	Natural abundance (%)	γ (MHz/T)
^{203}Tl	29.5	24.327
^{205}Tl	70.5	24.567
^{77}Se	7.5	8.13

where $K_{\rm iso}$ and $K_{\rm ax}$ are the isotropic and axial parts of the Knight shift, and θ is the angle between the magnetic field and the c axis. The spectra are well reproduced by convoluting with a Gaussian function. From the NMR spectra at several temperatures, $K_{\rm iso}$ and $K_{\rm ax}$ have been determined. The temperature dependence of $K_{\rm iso}$ is proportional to that of the static magnetic susceptibility, given by $K_{\rm iso}(T) = A_{hf}\chi(T)/(N_A\mu_B) + \chi_0$, with the hyperfine coupling constant $A_{\rm hf}$. Therefore, the linear slope in a $K(T)$ vs $\chi(T)$ plot gives the value of $A_{\rm hf}$. Here, having only a powder sample available, we have estimated the average hyperfine coupling constants using $K_{\rm iso}$ for the Tl and Se sites as a function of the susceptibility shown in Fig. 4. The $K(T)$ vs $\chi(T)$ for both Tl and Se sites is plotted, with temperature as an implicit parameter, in Fig. 11. Above 100 K, $\chi(T)$ follows a Curie-Weiss law with the full Yb^{3+} moment of $4.5\mu_B$, meaning that all CEF levels (four Kramers doublets) contribute to the susceptibility. On the other hand, below 100 K, only thermally populated low-energy CEF levels are contributing to the susceptibility and $A_{\rm hf}$ may be temperature dependent. Therefore, we used data only above 100 K and estimate $A_{\rm hf}$ as $+6.3$ and -4.1 kOe/μ_B for the Tl and Se sites, respectively. The hyperfine coupling for Se in $TlYbSe_2$ is of the same order, but slightly smaller than the hyperfine coupling in the related compound $NaYbSe_2$ [30]. Interestingly, the hyperfine coupling for the Tl site is one order of magnitude larger than the hyperfine coupling of Na in the related $NaYbSe_2$ compound [30]. This evidences the strong entanglement of Tl-based orbitals in the exchange paths of the $TlYbSe_2$ structure. It might be speculated that the enhancement of the Tl hyperfine coupling originates from the presence of the $6s^2$ lone pairs. This is also supported from the linewidth, which is much broader in the Tl case [Fig. 10(b)] in comparison to the Na case in $NaYbSe_2$ [30]. In the next section, we will describe the analysis of the Se-NMR data, focusing on the anisotropic nature of the hyperfine interaction and nuclear magnetic relaxation.

Since the Se nuclei are directly coupled to the Yb moments through the transferred hyperfine coupling due to the p-f mixing, ^{77}Se-NMR is a direct method to investigate the

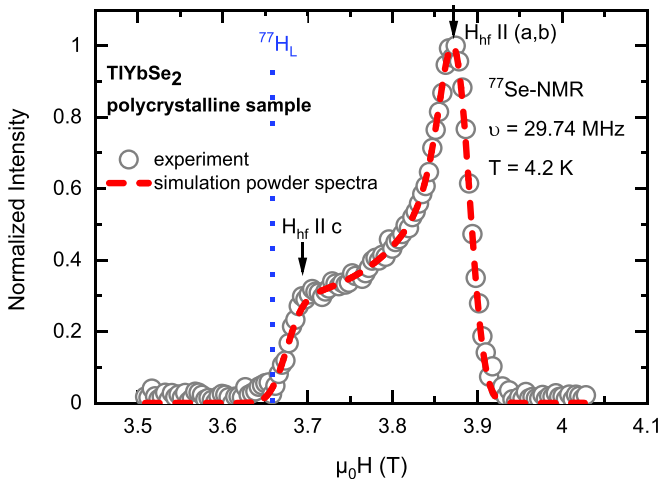


FIG. 12. Field-sweep ^{77}Se-NMR spectrum obtained at $T = 4.2$ K. The dashed line is a powder-spectrum simulation as described in the text. Arrows indicate hyperfine fields for fields along the c direction and perpendicular to c. The vertical dotted line indicates the Larmor field.

microscopic magnetic properties of the Yb network. Figure 12 shows a representative ^{77}Se-NMR spectrum, which can be reproduced by a typical powder pattern as mentioned above, and as shown by the red dashed line. It is well known that a uniaxial powder pattern has two cutoff fields at $H \parallel ab$ and $H \parallel c$, whose intensity ratio is 2:1. We define the Knight shifts for $H \parallel ab$ and $H \parallel c$ as K_{ab} and K_c, respectively. The determination of K_{ab} and K_c makes it possible to discuss the anisotropy of the local magnetic susceptibility even for a powder sample.

Figure 13 shows the temperature dependence of K_{ab} and K_c. The value of K_{ab} decreases with decreasing temperature, whereas K_c is almost independent of temperature. The observed anisotropy via the transferred hyperfine field at the Se site indicates that the local susceptibility of the Yb^{3+} moment

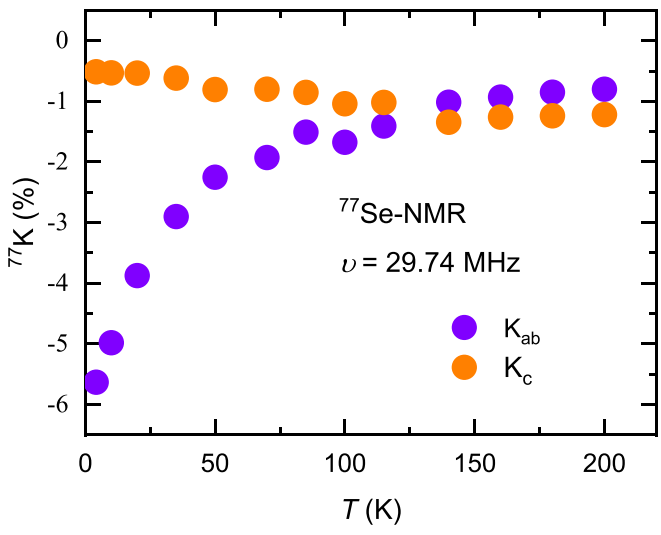


FIG. 13. Temperature dependence of the ^{77}Se Knight shifts, K_{ab} (purple) and K_c (orange).

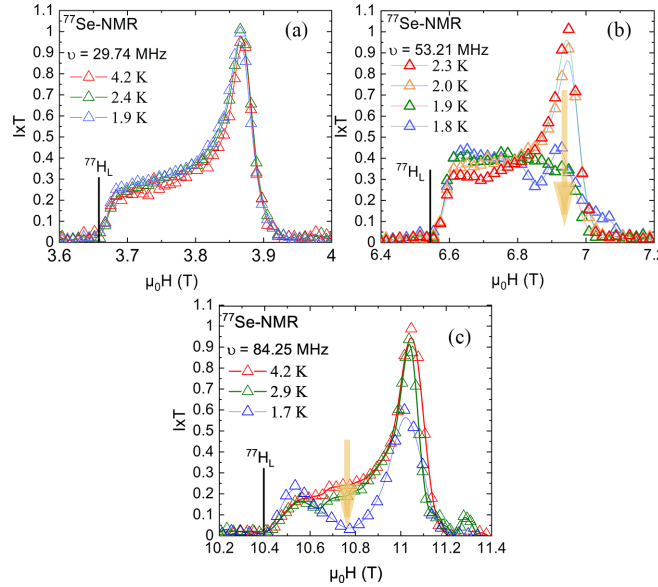


FIG. 14. ^{77}Se field-sweep NMR spectra of polycrystalline TlYbSe$_2$ at various temperatures at fixed frequencies of (a) 29.74 MHz, (b) 53.21 MHz, and (c) 84.52 MHz. Note that the effect of the temperature on the intensity is taken into account on the y axis (multiplication of integrated intensity with temperature). Vertical black solid lines indicate the Larmor field at that particular NMR frequency. The arrows indicate a loss of intensity due to anisotropic long-range magnetic order.

has a large anisotropy, corresponding to the anisotropy of the g factor as estimated from the ESR measurements (see Sec. III E). Moreover, the determination of $K_{ab}(T)$ and $K_c(T)$ yields valuable information about the anisotropy of the magnetic exchange interaction.

To investigate the mechanism of field-induced order observed in the magnetization and specific-heat measurements below 2.0 K, ^{77}Se-NMR spectra have been measured at several temperatures in the regime of the transition to long-range order. The ^{77}Se-NMR spectra at frequencies of $\nu = 29.74$, 53.21, and 84.52 MHz are shown in Figs. 14(a)–14(c), respectively. At 29.74 MHz, there is no change in the shape and intensity distribution of the spectra down to 1.9 K. At 53.21 MHz, the width of the intensity distribution does not change with temperature, but below 1.9 K, the intensity on the high-field side of the spectrum, corresponding to the $H \parallel ab$ component, strongly decreases. This reduction of the intensity may be attributed to a slowing down of the spin fluctuations of Yb^{3+} towards a magnetically ordered state. This slowing down gives rise to a shortening of the spin-lattice relaxation time T_1 and the spin-echo decay time T_2, which leads to a lowering of the signal intensity. For the ^{77}Se NMR of TlYbSe$_2$, only the spin fluctuations of the Yb^{3+} moments govern the T_1 relaxation since the ^{77}Se nuclear spin moment is $I = 1/2$, i.e., the nuclear electric quadrupole moment is zero. For a detailed investigation of the spin fluctuations of Yb^{3+}, we have measured the temperature dependence of T_1 at a fixed field $H = 6.95$ T and two different frequencies, $\nu = 53.21$ and 55.73 MHz, corresponding to the field components $H \parallel ab$ and $H \parallel c$, respectively.

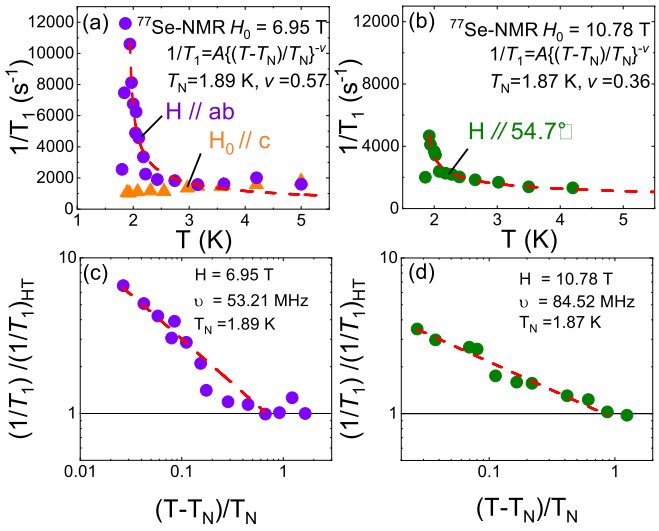


FIG. 15. (a) Temperature dependence of $(1/T_1)_{ab}$ (purple circles) and $(1/T_1)_c$ (orange triangles) at $H_0 = 6.95$ T and (b) of $(1/T_1)_{\rm ma}$ (ma: magic angle) (green circles) at H_0=10.78 T. The red dashed lines are results from least-squares fitting using Eq. (2) with $T_N = 1.89$ K, $v = 0.57$ at 6.95 T, and T_N =1.87 K, $v = 0.36$ at 10.78 T, respectively. (c),(d) Log-log plot of normalized $(1/T_1)/(1/T_1)_{HT}$ against reduced temperature $(T - T_N)/T_N$ at $\mu_0 H_0 = 6.95$ and 10.78 T, where T_N is set to 1.89 and 1.87 K, and $(1/T_1)_{HT}$ is the averaged value of $1/T_1$ above 3.0 and 3.5 K, respectively.

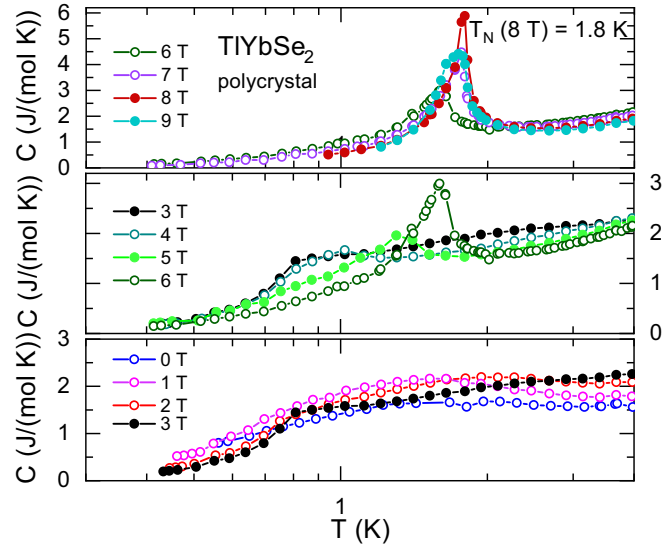


FIG. 16. Specific heat as function of temperature between 0.3 and 4 K in magnetic fields from 0 to 9 T as indicated.

The spectrum recorded at 84.25 MHz yields a reduction of the $H \parallel 54.7°$ component at 10.78 T. We have measured the temperature dependence of T_1 at this field.

The T_1 measurements were performed using the inversion-recovery method. The recovery of the nuclear magnetization is described by $M_0[1 - c_0 \exp(-t/T_1)^\beta]$ to obtain the T_1 values, where M_0, c_0, and β are the equilibrium value of the magnetization, the inversion parameter, and a stretching exponent, respectively. The $1/T_1$ are named $(1/T_1)_{ab}$, $(1/T_1)_c$, and $(1/T_1)_{\rm ma}$ for $H \parallel ab$, $H \parallel c$, and $H \parallel 54.7$ degree, respectively. The observed value of β in the paramagnetic state is 1, indicating that the T_1 relaxation is determined by spatially homogeneous spin fluctuations. Figure 15(a) shows the temperature dependence of $(1/T_1)_{ab}$ and $(1/T_1)_c$. Both are almost independent of temperature above 3.0 K. Below 3.0 K, $(1/T_1)_{ab}$ diverges with a critical slowing down of fluctuating Yb moments toward magnetic long-range order, whereas $(1/T_1)_c$ decreases linearly. This result indicates that spin fluctuations along the c axis are frozen because, for that configuration, $1/T_1$ probes the spin fluctuations perpendicular to the magnetic field.

From the temperature dependence of $(1/T_1)_{ab}$, T_N and the critical exponent v are determined as 1.89 K and 0.57, respectively, fitting the data using the following equation:

$$\frac{1}{T_1} = A\left[\frac{T - T_N}{T_N}\right]^{-v}, \qquad (2)$$

where A is a constant and v is the critical exponent. To find the optimal value of T_N, we normalized $1/T_1$ to its high-temperature value as $(1/T_1)/(1/T_1)_{HT}$ and plotted it against the reduced temperature $(T - T_N)/T_N$ in a log-log plot in Fig. 15(c). When a trial value of T_N is put in Eq. (2), $\delta v/v$ is estimated by a least-squares fit of $(1/T_1)/(1/T_1)_{HT}$, where δv is the error of v. When $\delta v/v$ reaches a minimum, we extract T_N and v. Similarly, we determined $T_N = 1.87$ K and $v = 0.36$, as shown in Figs. 15(b) and 15(d). The critical exponent provides us with information on how the antiferromagnetic correlations diverge at T_N. In mean-field theory, v=1/2. The theory value for a three-dimensional isotropic Heisenberg model is $v = 1/3$ [35]. The critical exponent $v = 0.57$ and 0.36 indicates that the magnetic order at 6.95 and 10.78 T is explained by a three-dimensional critical regime, respectively. Thus, although the Yb moments are arranged in a triangular lattice of two-dimensional planes with pronounced Yb spin anisotropy, the fluctuations are three dimensional (3D) in nature.

G. Specific heat as function of temperature and field

Measurements of the specific heat of polycrystalline $TlYbSe_2$ clearly show the evolution of magnetic order with increasing magnetic field. While in fields up to 2 T, there is only a broad maximum, from 3 T, a step develops, which then forms a peak at 5 T. This peak becomes narrower as the field increases. The peak is most pronounced at 8 T, which evidences a maximum ordering temperature of $T_N = 1.8$ K (Figs. 16 and 17). Already at 9 T, the peak starts to broaden and shifts to slightly lower temperatures. An additional, step-like anomaly develops, which shifts with increasing field to lower temperatures, while the peak at high temperatures is robust in the field, i.e., hardly shifts but clearly loses intensity.

Such a behavior was also found in polycrystalline samples of the relative $NaYbO_2$. This is probably due to the anisotropy of the field-induced order, which occurs here in a powder average. Single-crystalline samples, such as $NaYbS_2$ and $NaYbSe_2$, show the development of the field-induced order for in-plane magnetic fields. Here, for $TlYbSe_2$, our ^{77}Se NMR also clearly evidences a field-induced order only for in-plane fields [see Fig. 14(b)].

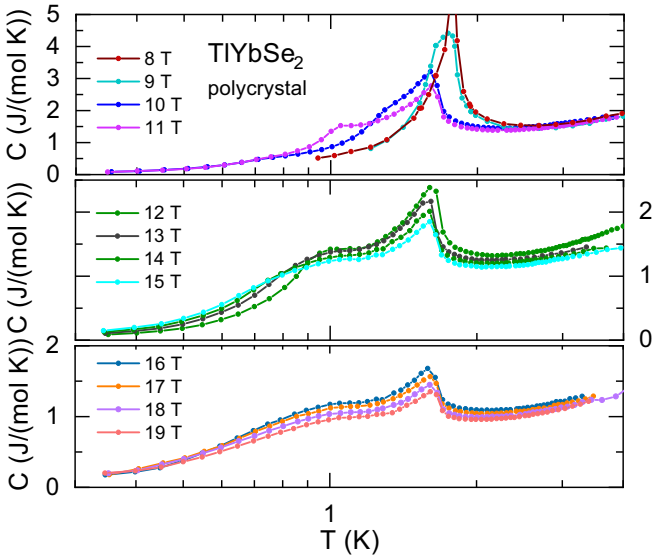


FIG. 17. Specific heat as function of temperature between 0.3 and 4 K in magnetic fields from 8 to 19 T as indicated.

Isothermal specific-heat measurements as a function of field in the vicinity of the maximum ordering temperature of about 1.8 K are shown in Fig. 18. A steplike structure indicates the formation of magnetic order. At 1.82 K, the specific heat has a pronounced peak at about 8 T. At temperatures above 1.82 K, the peak disappears. We take this as strong evidence for the emergence of a field-induced magnetic order. Interestingly, the specific heat has a small maximum at much smaller fields at about 1.5 T, which is robust in the temperature range between 1.7 and 2 K (Fig. 19). This might be related to an effect of the magnetic field on residual fluctuations in the disordered spin-liquid-like regime of the phase diagram.

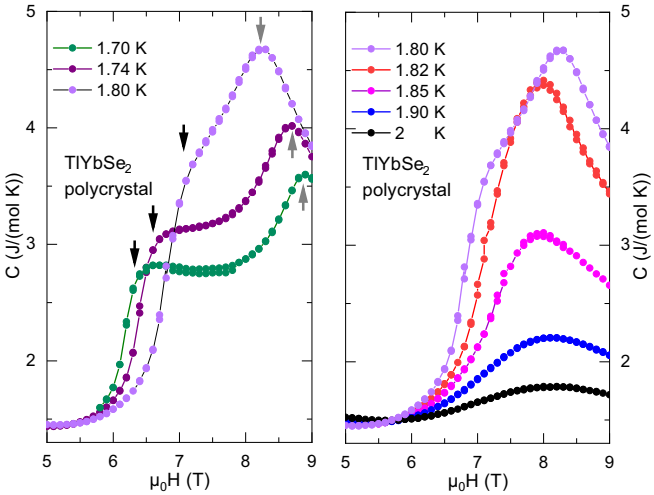


FIG. 18. Specific heat as function of magnetic field between 5 and 9 T at temperatures indicated. The arrows indicate crossover fields to the field-induced long-range ordered state.

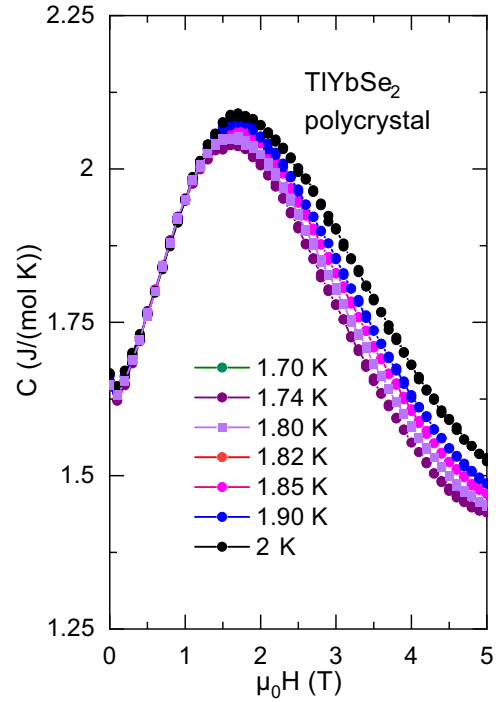


FIG. 19. Specific heat as a function of magnetic fields between 0 and 5 T at the indicated temperatures.

H. Alternating current (ac) susceptibility at very low temperatures

To prove the absence magnetic order down to rather low temperatures, we performed ac susceptibility measurements down to a temperature of 0.05 K. The measurements were carried out in zero field and in fields of 0.05 T and 0.2 T (see Fig. 20). There is no evidence of magnetic order. The decrease in susceptibility with increasing field may indicate a suppression of intrinsic critical fluctuations in the spin-liquid state. Critical fluctuations inherent to the spin-liquid state are evidenced for NaYbSe$_2$ from Se-NMR data in [30] and in Muon experiments [36].

IV. *H-T* PHASE DIAGRAM AND CONCLUSION

Figure 21 shows the H-T phase diagram of polycrystalline TlYbSe$_2$, obtained by the various methods used in this work. As for other triangular-lattice Yb delafossite systems, such as NaYbSe$_2$ [7,30] and CsYbSe$_2$ [12], magnetic order is absent at zero field, which suggests a quantum spin-liquid ground state. Upon applying magnetic field, magnetic order is induced.

In contrast to all the other alkaline-metal (AM)-based $R\bar{3}m$ Yb delafossites AMYbCh$_2$ (AM = Na, K, Rb, Cs), the maximum ordering temperature exceeds 1 K and reaches 1.8 K at about 8 T. Furthermore, the saturation field is significantly increased from 10 T to about 20 T for TlYbSe$_2$. We claim that this originates from a polarization of the Tl-based $6s^2$ lone pairs by the spatially extended Se-based $4p$ orbitals. These Se $4p$ orbitals are also involved in the Yb-Se-Yb in-plane superexchange via $4f$ orbitals, which drives the two-dimensional magnetism of the system. For

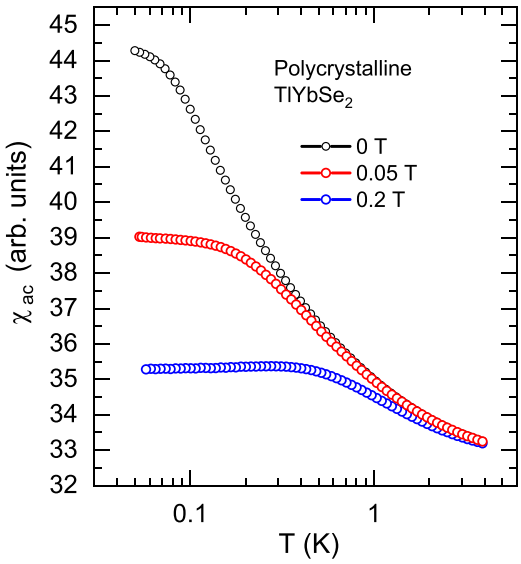


FIG. 20. Low-temperature ac susceptibility as a function of temperature in arbitrary units. Measurements are performed with an alternating magnetic field of 0.3 mT at a frequency of 4 kHz in the field-cooled mode. The temperature was stabilized for each individual data point. Note that the data were not corrected for extrinsic (e.g., sample holder) temperature-independent offset terms.

example, such an effect was observed in the case of the Tl-based trivanadate TlV_3O_8 [37]. Here, compared to RbV_3O_8, the ordering temperature and strength of the superexchange were increased by Tl-based $6s^2$ lone pairs. Our final conclusion is that even though there is a strong spin anisotropy, as evidenced by our ESR and NMR results, the exchange anisotropy and the fluctuations are more three dimensional

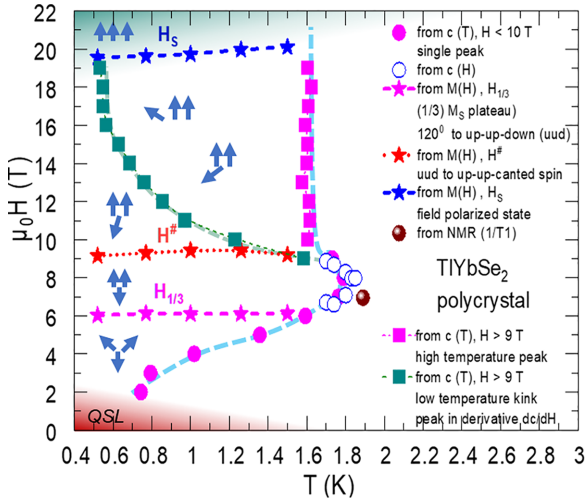


FIG. 21. H-T phase diagram of polycrystalline $TlYbSe_2$, obtained by the various methods presented in this work. The dashed lines are a guide for the eyes. The colored areas indicate the two extreme regimes: a quantum spin liquid (QSL) at zero field and a fully polarized state above about 20 T. As the magnetic field is increased above the QSL regime, a 120 degree order manifests (up to $H_{1/3}$), followed by the uud (up to $H^{\#}$) and uu-canted phases. At very high fields (H_S), all spins are polarized.

in nature in $TlYbSe_2$. Overall, this strengthens the antiferromagnetic coupling, while maintaining strong frustration and the emergence of the putative spin-liquid ground state at zero field.

Further field- and temperature-dependent single-crystal studies on the magnetic anisotropy by magnetization, specific-heat, and NMR measurements are required to complete the picture sketched above. Nonetheless, the comprehensive results presented here reveal the impact of the monovalent ion on the exchange physics and identify Tl-based Yb delafossites as a different fascinating subclass of triangular-lattice spin liquids.

ACKNOWLEDGMENTS

We thank H. Yasuoka for discussions of the NMR results and Pierre Chailloleau for support on the ESR measurements. Further thanks goes to B. Schmidt for fruitful discussions on the theory of magnetic exchange in 4*f* triangular lattices. We thank E. Häußler for help in sample preparation at the beginning of the project. We acknowledge the support from the Deutsche Forschungsgemeinschaft (DFG) through SFB 1143 (Project ID No. 247310070) and the Würzburg-Dresden Cluster of Excellence on Complexity and Topology in Quantum Matter - ct.qmat (EXC 2147, Project ID No. 390858490). A.M.S. thanks the FRC/URC of UJ, and the SA-NRF (Grant No. 105702) for financial assistance. Further, we acknowledge the support of the HLD at HZDR, member of the European Magnetic Field Laboratory (EMFL).

DATA AVAILABILITY

The data that support the findings of this article are openly available [38].

APPENDIX A: BAND STRUCTURE

Figure 22 shows a comparison of the the band structures of $TlYbSe_2$ and $KYbSe_2$. Figure 23 labels the high-symmetry points in the Brillouin zone. Although both Tl and K are formally monovalent, the band structures of both compounds are surprisingly different. The most obvious difference is the

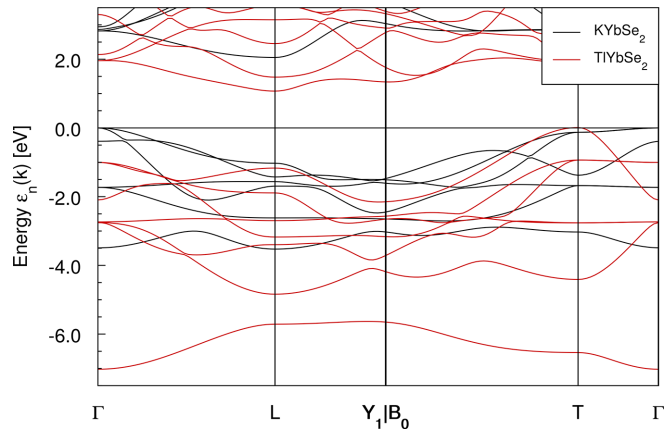


FIG. 22. Band structures of $TlYbSe_2$ and $KYbSe_2$. The Fermi level is at zero energy. To facilitate a comparison, the Brillouin zone of $KYbSe_2$ is rescaled to match the one of $TlYbSe_2$.

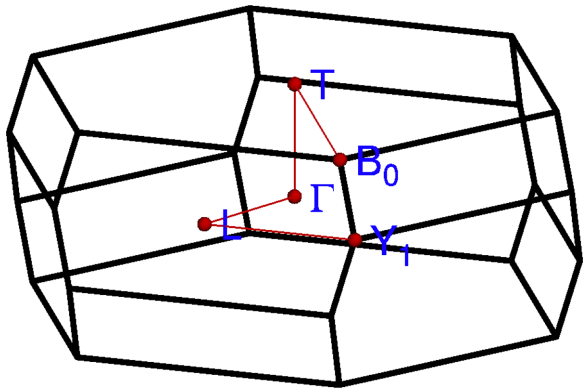


FIG. 23. Illustration of the first Brillouin zone with the high-symmetry points of the band structure calculation.

much larger valence-band width of the Tl compound, which is almost twice as large as the structurally very similar K system. The underlying reason is the strong hybridization of the Se 4*p* states with the Tl 6*s* lone pair. This leads to the bonding band at low energies between about −5.5 and −7 eV. Due to the hybridization, its band width of about 1.5 eV is far from a localized state. In consequence, the corresponding antibonding band with dominating Se contribution is split to the top of the valence band, causing a change in the order of the bands compared to the K compound. This is best seen along the Γ-*T* direction, corresponding to the crystallographic direction between the YbSe$_2$ planes. The dispersion of these Tl-Se related bands is considerably larger than that of the bands in KYbSe$_2$, in this way also being responsible for the larger magnetic couplings in the Tl compound.

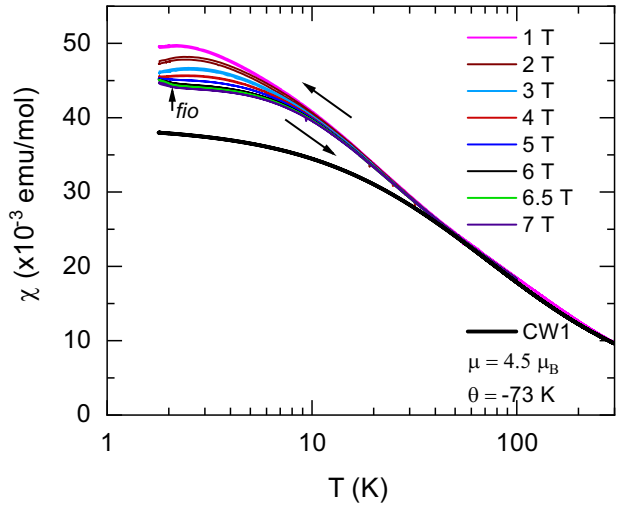


FIG. 24. Susceptibility as a function of temperature, obtained at various magnetic fields as indicated. The arrows indicate whether measurements were taken during warming up (zero-field cooling, zfc) or cooling down (field cooling). The vertical arrow marks the onset of field-induced order (fio) for fields above approximately 5 T.

APPENDIX B: SUSCEPTIBILITY AT VARIOUS FIELDS

The temperature-dependent susceptibility at various fields is plotted in Fig. 24. Above approximately 5 T, an upturn in the susceptibility can be observed at about 2 K. We interpret this as a signature of the field-induced magnetic order, in good agreement with the results of the heat capacity.

[1] M. A. Marquardt, N. A. Ashmore, and D. P. Cann, Crystal chemistry and electrical properties of the delafossite structure, Thin Solid Films **496**, 146 (2006).

[2] A. P. Mackenzie, The properties of ultrapure delafossite metals, Rep. Prog. Phys. **80**, 032501 (2017).

[3] J. P. Doumerc, A. Wichainchai, A. Ammar, M. Pouchard, and P. Hagenmuller, On magnetic-properties of some oxides with delafossite-type structure, Mater. Res. Bull. **21**, 745 (1986).

[4] A. P. Ramirez, Geometrical frustration, Handbook Magnet. Mater. **13**, 423 (2001), Chap. 4.

[5] M. Baenitz, Ph. Schlender, J. Sichelschmidt, Y. A. Onykiienko, Z. Zangeneh, K. M. Ranjith, R. Sarkar, L. Hozoi, H. C. Walker, J. C. Orain, H. Yasuoka, J. van den Brink, H. H. Klauss, D. S. Inosov, and Th. Doert, NaYbS$_2$: A planar spin-1/2 triangular-lattice magnet and putative spin liquid, Phys. Rev. B **98**, 220409 (2018).

[6] K. M. Ranjith, D. Dmytriieva, S. Khim, J. Sichelschmidt, S. Luther, D. Ehlers, H. Yasuoka, J. Wosnitza, A. A. Tsirlin, H. Kühne, and M. Baenitz, Field-induced instability of the quantum spin liquid ground state in the $J_{\text{eff}} = 1/2$ triangular-lattice compound NaYbO$_2$, Phys. Rev. B **99**, 180401(R) (2019).

[7] K. M. Ranjith, S. Luther, T. Reimann, B. Schmidt, Ph. Schlender, J. Sichelschmidt, H. Yasuoka, A. M. Strydom, Y. Skourski, J. Wosnitza, H. Kühne, Th. Doert, and M. Baenitz, Anisotropic field-induced ordering in the triangular-lattice quantum spin liquid NaYbSe$_2$, Phys. Rev. B **100**, 224417 (2019).

[8] W. Liu, Z. Zhang, J. Ji, Y. Liu, J. Li, X. Wang, H. Lei, G. Chen, and Q. Zhang, Rare-earth chalcogenides: A large family of triangular lattice spin liquid candidates, Chin. Phys. Lett. **35**, 117501 (2018).

[9] B. Schmidt, J. Sichelschmidt, K. M. Ranjith, Th. Doert, and M. Baenitz, Yb delafossites: Unique exchange frustration of 4*f* spin-1/2 moments on a perfect triangular lattice, Phys. Rev. B **103**, 214445 (2021).

[10] M. Xie, W. Zhuo, Y. Cai, Z. Zhang, and Q. Zhang, Rare-earth chalcogenides: An inspiring playground for exploring frustrated magnetism, Chin. Phys. Lett. **41**, 117505 (2024).

[11] A. V. Chubukov and D. I. Golosov, Quantum-theory of an antiferromagnet on a triangular lattice in a magnetic-field, J. Phys.: Condens. Matter **3**, 69 (1991).

[12] T. Xie, A. A. Eberharter, J. Xing, S. Nishimoto, M. Brando, P. Khanenko, J. Sichelschmidt, A. A. Turrini, D. G. Mazzone, P. G. Naumov, L. D. Sanjeewa, N. Harrison, A. S. Sefat, B. Normand, A. M. Laeuchli, A. Podlesnyak, and S. E. Nikitin, Complete field-induced spectral response of the

spin-1/2 triangular-lattice antiferromagnet $CsYbSe_2$, npj Quantum Mater. **8**, 48 (2023).

[13] J. Xing, L. D. Sanjeewa, J. Kim, G. R. Stewart, M.-H. Du, F. A. Reboredo, R. Custelcean, and A. S. Sefat, Crystal synthesis and frustrated magnetism in triangular lattice $CsRESe_2$ (RE = La-Lu): Quantum spin liquid candidates $CsCeSe_2$ and $CsYbSe_2$, ACS Mater. Lett. **2**, 71 (2020).

[14] T. Ferreira, J. Xing, L. D. Sanjeewa, and A. S. Sefat, Frustrated magnetism in triangular lattice $TlYbS_2$ crystals grown via molten flux, Front. Chem. **8**, 00127 (2020).

[15] Y. Skourski, M. D. Kuz'min, K. P. Skokov, A. V. Andreev, and J. Wosnitza, High-field magnetization of Ho_2Fe_{17}, Phys. Rev. B **83**, 214420 (2011).

[16] T. Gruner, J. Wykhoff, J. Sichelschmidt, C. Krellner, C. Geibel, and F. Steglich, Anisotropic electron spin resonance of $YbIr_2Si_2$, J. Phys.: Condens. Matter **22**, 135602 (2010).

[17] S. Kabré, M. Julien Pouzol, and M. Guittard, Étude cristallographique des combinaisons ternaires formées par le thallium, les terres rares et le soufre, le sélénium ou le tellure, le long des binaires TL_2X-L_2X_3, Bull. Soc. Chim. Fr. **9-10**, 1881 (1974).

[18] M. Duczmal and L. Pawlak, Magnetic and structural characterization of $TlLnSe_2$ compounds (Ln: Nd to Yb), J. Alloys Compd. **225**, 181 (1995).

[19] A. Szczerbakow and K. Durose, Self-selecting vapour growth of bulk crystals – Principles and applicability, Prog. Cryst. Growth Charact. Mater. **51**, 81 (2005).

[20] J.-Q. Yan and M. A. McGuire, Self-selecting vapor growth of transition-metal-halide single crystals, Phys. Rev. Mater. **7**, 013401 (2023).

[21] A. A. Coelho, Topas and topas-academic: An optimization program integrating computer algebra and crystallographic objects written in C++, J. Appl. Crystallogr. **51**, 210 (2018).

[22] A. A. Coelho, TOPAS Academic V4.1 Technical Reference (unpublished).

[23] Bruker, *APEX Suite V.##* (Bruker AXS Inc., Madison, WI, 2016).

[24] G. M. Sheldrick, A short history of SHELXL, Acta Crystallogr. Sect. A **64**, 112 (2008).

[25] G. M. Sheldrick, Crystal structure refinement with SHELXL, Acta Crystallogr. C **71**, 3 (2015).

[26] Y. Li, G. Chen, W. Tong, L. Pi, J. Liu, Z. Yang, X. Wang, and Q. Zhang, Rare-earth triangular lattice spin liquid: A single-crystal study of $YbMgGaO_4$, Phys. Rev. Lett. **115**, 167203 (2015).

[27] J. Sichelschmidt, P. Schlender, B. Schmidt, M. Baenitz, and T. Doert, Electron spin resonance on the spin-1/2 triangular magnet $NaYbS_2$, J. Phys.: Condens. Matter **31**, 205601 (2019).

[28] J. Sichelschmidt, B. Schmidt, P. Schlender, S. Khim, T. Doert, and M. Baenitz, Effective spin-1/2 moments on a Yb^{3+} triangular lattice: An ESR study, JPS Conf. Proc. **30**, 011096 (2020).

[29] F. Grußler, M. Hemmida, S. Bachus, Y. Skourski, H.-A. Krug von Nidda, P. Gegenwart, and A. A. Tsirlin, Role of alkaline metal in the rare-earth triangular antiferromagnet $KYbO_2$, Phys. Rev. B **107**, 224416 (2023).

[30] S. Luther, K. M. Ranjith, Th. Doert, J. Wosnitza, H. Kühne, and M. Baenitz, Anisotropic magnetism and spin fluctuations in the triangular-lattice spin-liquid candidate $NaYbSe_2$: A single-crystal ^{23}Na and ^{77}Se NMR study, Phys. Rev. B **110**, 214440 (2024).

[31] T. Förster, F. A. Garcia, T. Gruner, E. E. Kaul, B. Schmidt, C. Geibel, and J. Sichelschmidt, Spin fluctuations with two-dimensional *xy* behavior in a frustrated $s = \frac{1}{2}$ square-lattice ferromagnet, Phys. Rev. B **87**, 180401(R) (2013).

[32] H. Benner and J. P. Boucher, Spin dynamics in the paramagnetic regime: NMR and EPR in two-dimensional magnets, in *Physics and Chemistry of Materials with Low-Dimensional Structures*, Vol. 9, edited by L. J. De Jongh (Kluwer, Dordrecht, 1990), Chap. Magnetic properties of layered transition metal compounds, pp. 323–378.

[33] R. Orbach and B. Bleaney, Spin-lattice relaxation in rare-earth salts field dependence of the two-phonon process, Proc. Roy. Phys. Soc. A **264**, 485 (1961).

[34] A. Abragam and B. Bleaney, *Electron Paramagnetic Resonance of Transition Ions* (Clarendon Press, Oxford, 1970).

[35] B. Halperin and P. C. Hohenberg, Generalization of scaling laws to dynamical properties of a system near its critical point, Phys. Rev. Lett. **19**, 700 (1967).

[36] Z. Zhang, J. Li, M. Xie, W. Zhuo, D. T. Adroja, P. J. Baker, T. G. Perring, A. Zhang, F. Jin, J. Ji, X. Wang, J. Ma, and Q. Zhang, Low-energy spin dynamics of the quantum spin liquid candidate $NaYbSe_2$, Phys. Rev. B **106**, 085115 (2022).

[37] G. Agbeworvi, W. Zaheer, J. D. D. Ponis, J. V. V. Handy, J. R. R. Ayala, J. L. L. Andrews, P. Schofield, C. Jaye, C. Weiland, D. A. A. Fischer, and S. Banerjee, Effect of stereochemically active electron lone pairs on magnetic ordering in trivanadates, Inorg. Chem. **62**, 12965 (2023).

[38] M. Baenitz, Data related to the manuscript entitled $TlYbSe_2$ as a new member of the $J = 1/2$ triangular lattice Yb delafossite family: From spin liquid to field-induced magnetic order, Edmond (2025), https://doi.org/10.17617/3.NIGLVV.